Nanoscale

COMMUNICATION

View Article Online
View Journal | View Issue

Cite this: *Nanoscale*, 2018, **10**, 13310

Received 12th April 2018,
Accepted 21st June 2018

DOI: 10.1039/c8nr02956c

rsc.li/nanoscale

Variable segment roles: modulation of the packing modes, nanocrystal morphologies and optical emissions†

Sha-Sha Wang, ‡[a] Rong Rong,‡[a] Ling-Zhi Jin,[a] Shan-Shan Yang,[a] Yin-Xiang Li,[a] He Zhang,[a] Yu-Wei Xiong,[b] Li-Tao Sun, [b] Hong-Tao Cao,[a] Ling-Hai Xie *[a] and Wei Huang *[a,c]

Three isomers were prepared by covalently grafting carbazole (Cz) onto spiro[fluorene-9,9′-xanthene] (SFX) at different positions. Due to the complicated and variable roles of molecular segments, an evolution of the corresponding molecular packing mode was realized, accompanied by the change of nanocrystal morphology and photoluminescence properties.

Organic semiconductors have attracted great interest as critical components in future optoelectronic devices.[1] Their electronic, excitonic and photonic properties,[2] including anisotropic carrier transport,[3] optical waveguides[4] and delayed fluorescence[5] are strongly dependent on the condensed states of the organic molecules, namely molecular arrangements, crystalline structures, morphologies, and dimensions. To harvest higher charge carrier mobility in preferential directions, precise control over molecular packing motifs as 1D π-stacking, 2D herringbone/brickwork packing[6] and the packing lattice[7] is significant for organic field-effect transistor (OFET) applications.[8] For light emission, face-to-face stacking (H-aggregation) of molecular dipoles would often lead to aggregation-caused quenching.[9] In the case of staggered stacking (J-aggregation) or crossed stacking (X-aggregation),[10] luminescence quenching could be effectively inhibited due to diminished dipole–dipole interactions.[11] Asymmetric photon transport was observed in 2-acetyl-6-methylaminonaphthalene (AMN) nanosheets, which is determined by the direction of the transition dipoles.[12] Therefore, manipulating the self-assembly behavior of organic molecules to achieve desired molecular aggregations is of significant importance.

Extensive efforts have been made to control the assembly by tailoring the organic molecular structures, such as adding different side substituents;[12,13] varying the isomerism;[7,14] introducing heteroatoms[15] and so on.[16] However, a rational molecular design rather than empirical experimentation is still lacking. Based on the deep understanding of the molecular four-element structure,[17] our design strategy is to introduce a pair of opposite characteristics (attractive supramolecular interaction and steric repulsion) into one molecular system, which was named synergistically molecular attractor–repulsor theory (SMART). The first SMART molecule spiro[fluorene-9,7′-dibenzo[*c*,*h*]acridine]-5′-one (Py-SFDBAO) was reported in 2013 which adopted a novel 2D interdigital assembly mode to form ultrathin nanosheets.[18] Then another model molecule *N*,*N*-diphenyl-4-(9-phenyl-fluoren-9-yl) phenylamine (TPA-PF) demonstrated that the interdigital molecular arrangement is a result of the cooperative effect of the attractive supramolecular segment (SS) TPA and the repulsive bulky group (BG) PF. Similar to the lipid bilayer, TPA connected with each other in the middle of the layer due to the abundant supramolecular interactions, and bulky PF lined on both sides. This interdigital lipid bilayer-like (ILB) packing is proved to be an assembly paradigm for SS–BG molecules, indicating that SMART is general and effective for molecular design.[19]

Nevertheless, considering the multiplicity and variability of the molecular segment's roles, to fully define and clarify the attractor/repulsor or other kinds of segments is necessary for the precise control of assembly and would further improve SMART. Here, three isomers were synthesized by covalently grafting carbazole (Cz) onto spiro[fluorene-9,9′-xanthene] (SFX) at different positions (SFX-2-Cz, SFX-3′-Cz and SFX-2′-Cz). A comparison of their molecular crystal structures and packing motifs reveals that the function of the same segment (Cz or

[a]*Centre for Molecular Systems and Organic Devices (CMSOD), Key Laboratory for Organic Electronics and Information Displays & Jiangsu Key Laboratory for Biosensors, Institute of Advanced Materials (IAM), Jiangsu National Synergetic Innovation Center for Advanced Materials (SICAM), Nanjing University of Posts & Telecommunications (NUPT), 9 Wenyuan Road, Nanjing 210023, P.R. China. E-mail: iamlhxie@njupt.edu.cn*

[b]*SEU-FEI Nano-Pico Center and Key Lab of MEMS of Ministry of Education, School of Electronic Science and Engineering, Southeast University, 2 Sipailou, Nanjing 210096, P. R. China*

[c]*Shaanxi Institute of Flexible Electronics (SIFE), Northwestern Polytechnical University (NPU), 127 West Youyi Road, Xi'an 710072, P.R. China. E-mail: wei-huang@njtech.edu.cn*

†Electronic supplementary information (ESI) available. See DOI: 10.1039/c8nr02956c

‡These authors contributed equally to this work.

SFX) in different isomers varies. In SFX-3′-Cz and SFX-2′-Cz, bulky SFX could be attractive other than the presupposed role as a pure repulsor. The variable roles of the molecular segments induce the transformation of assembly and nanocrystal morphologies, and finally manipulate the solid state luminescence. Three kinds of combinations of supramolecular interaction and steric hindrance in bulk-plane molecules were investigated systematically, revealing how the gradual change of the segment's roles would influence the assembly evolution as well as the dependent properties, which may further enrich SMART for the rational molecular design.

In general, the design of the SS–BG molecule is to integrate a steric group (with SP3 carbon atom) and a functional group (with heteroatoms or conjugated rings) into one molecule. In this work, we prepared three isomers with the same SFX and Cz groups: SFX-2-Cz, SFX-3′-Cz and SFX-2′-Cz, according to their different linkage positions. The synthetic routes along with the ^{1}H and ^{13}C NMR spectra are listed in ESI Fig. S1,† and their chemical molecular structures are shown in Fig. 1a–c. To explore more information on their steric architectures and supramolecular interaction distributions, single crystals of the isomers were obtained through a solvent diffusion method (the single crystal data are shown in Table S1†). The molecular crystal structures in Fig. 1d–f reveal that the space configurations of the steric cruciform-shaped SFX (marked in blue) in these isomers are almost the same with the corresponding dihedral angle between the fluorene plane and xanthene plane as 88.3°, 89.4° and 88.7°. However, the locations of the supramolecular interaction sites undergo a gradual change in the isomers, inducing the role variety of the segments. SFX-2-Cz is a normal SS–BG molecule with Cz providing most of the supramolecular interactions and SFX mainly presenting steric repulsion as expected. For SFX-3′-Cz, the supramolecular interaction sites are distributed on both Cz and SFX, thus SFX is endowed with supramolecular interaction and steric hindrance simultaneously and defined as the supramolecular bulky group (SBG). In SFX-2′-Cz, all the supramolecular forces are contributed by SFX, meanwhile the Cz group only acts as a planar segment (PS) without any obvious supramolecular interactions or steric hindrance. The schematic diagrams of SFX-2-Cz, SFX-3′-Cz and SFX-2′-Cz in Fig. 1g–i vividly indicate the distinct segment's role attributes as SS–BG molecule, SS–SBG molecule and PS–SBG molecule, respectively.

Due to the periodic arrangement of molecules on the nanometer scale, a nanocrystal is an ideal platform to investigate the relationship between the molecular stacking and the photoelectrical properties. The morphologies and structures of the isomers' nanocrystals prepared with the surfactant Pluronic P123 are shown in Fig. 2a–f and Fig. S2† by scanning electron microscopy (SEM), transmission electron microscopy (TEM) and atomic force microscopy (AFM). At first glance, SFX-2-Cz and SFX-3′-Cz exhibit a 2D nanosheet feature, while SFX-2′-Cz is in a 1D rod shape, which are closely related to the corresponding molecular packing modes. Under SEM and TEM observation, the nanocrystals displayed regular outlines with distinct edges/corners, and the details of the two sharp ends are shown in Fig. 2c (inset). The sizes are measured as follows: SFX-2-Cz parallelograms (*ca.* 1 ± 0.2 μm in length, 0.7 ± 0.2 μm in width, 37 nm in thickness), SFX-3′-Cz rhombuses (*ca.* 7.1 ± 1.7 μm in length, 11 nm in thickness) and SFX-2′-Cz rods (14.2 ± 2.7 μm in length, 32 ± 6 nm in width, 156 nm in height). The X-ray powder diffraction (XRD) patterns of the nanocrystals are in good agreement with their single crystal XRD pattern, as shown in Fig. S3.† The appearance of the (001) reflections for SFX-2-Cz parallelograms and the (*h*00) reflections for SFX-3′-Cz rhombuses demonstrates their layered structures with *d*-spacings of 17.9 Å and 11.6 Å. Selected-area

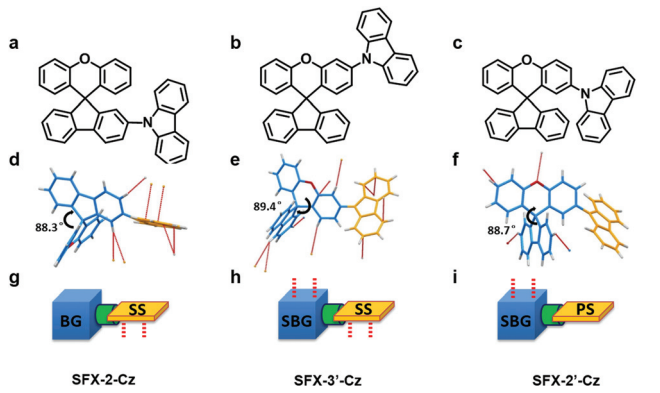

Fig. 1 Chemical molecular structures, single crystal structures and schematic diagrams with the supramolecular force distribution. (a–c) The chemical structures of SFX-2-Cz, SFX-3′-Cz and SFX-2′-Cz. (d–i) The molecular crystal structures and the corresponding molecular models of SS–BG, SS–SBG and PS–SBG for SFX-2-Cz, SFX-3′-Cz and SFX-2′-Cz, respectively. (The blue block and yellow part in (g–i) represent the SFX and Cz groups, respectively. The green region acts as a covalent linkage between the two parts. The red dotted lines represent the supramolecular force sites.)

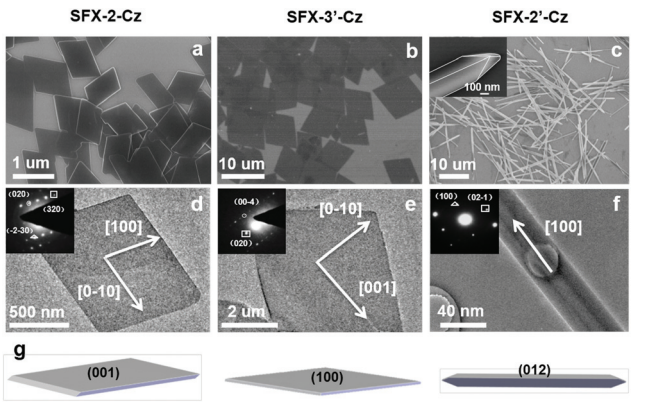

Fig. 2 (a–c) SEM and (d–f) TEM images of 2D parallelograms, 2D rhombuses and 1D rods aggregated from SFX-2-Cz, SFX-3′-Cz and SFX-2′-Cz, respectively. The insets of (d–f): Corresponding SAED pattern of a single nanocrystal and the electron beam directions are [001], [100] and [012], respectively. (g) Schematic models of the three nanostructures calculated using WinXMorph software based on the results of SAED and crystal parameters.

electron diffraction (SAED) patterns (insets in Fig. 2d–f) further verify that all the spots of the nanocrystals can be indexed to the corresponding single crystal structures, and the axial growth directions are also confirmed by the white arrows indicated in the TEM images. According to the structure characterization, the simulated models of SFX-2-Cz, SFX-3′-Cz and SFX-2′-Cz nanocrystals by means of WinXMorph software are shown in Fig. 2g with the indices of the exposed crystal faces.

Nanocrystals of the three isomers formed without the assistance of a surfactant were studied to check the effect of P123, as displayed in Fig. S4.† From the comparison we could find that although the surfactant-assisted counterparts seem to be more uniform and clear, the corresponding surfactant-free samples have similar morphologies, indicating the molecular structures rather than surfactants dominating the crystallization. In addition, variations of other external conditions such as isomer concentrations, surfactant concentrations and the volume ratio of THF/water were performed as shown in Fig. S5–7.† No matter how the external conditions change, the final morphologies still retain the intrinsic features, which further proves the essential role of molecular characters.

To gain deeper insight into the hierarchical relationships from molecular structure to molecular packing to nanocrystals, the representative packing motifs of SFX-2-Cz, SFX-3′-Cz and SFX-2′-Cz are analyzed in Fig. 3. As expected, SFX-2-Cz molecules adopt a typical ILB packing due to the SS–BG molecular feature, as shown in Fig. 3a. The molecular packing in three axis directions as well as the respective supramolecular interaction analysis are disclosed in Fig. S8 and S9.† As viewed from the [010] crystal direction, a SFX-2-Cz trimer as the representative repeating unit exhibits the interdigital packing motif, that is supramolecular interactions concentrated on the middle Cz and repulsive SFX arranged on both sides. The interdigital chain extends along the [100] direction with strong π–π (3.38 Å in distance) and C–H···π (2.72 Å and 2.80 Å in distance) interactions. The stacking in the [010] direction continues to be in the interdigital molecular packing linked by van der Waals forces (2.12 Å in distance), thus the *ab* plane could be taken as a sandwich-like monolayer with the Cz network capped by SFX. Owing to the lack of obvious interactions in the [001] direction, there are explicit boundaries between the monolayers without any intersections and the growth along [001] is limited. The thickness of the monolayer is found to be 1.79 nm, which is identical to the *d*-spacing of the (001) crystal face, indicating the direct relationship between molecular arrangement and crystalline nanostructures.

For SFX-3′-Cz, the increasing of supramolecular interaction sites on bulky SFX induces the packing transformation from the paradigmatic ILB packing. A similar repeating trimer with an interdigital motif is still available for the noncovalent molecular chain propagation by C–H···π interactions (2.88 Å and 2.76 Å in distance) along the [010] direction, as shown in Fig. 3b and Fig. S10a.† Unlike the parallel arrangement of SFX-2-Cz chains into a clearly defined monolayer, SFX-3′-Cz molecular chains are staggered with each other because of the additional supramolecular interaction sites on SFX groups facilitating a more closer packing mode (Fig. S10b†). Consequently, the stacking layer in the *bc* plane looks grooved (Fig. S10c†) and the corresponding (100) spacing is 1.16 nm, which is much smaller than the SFX-2-Cz counterpart (1.79 nm) due to the intersection between the layers. The specific supramolecular interactions along the [010] and [001] directions are displayed in Fig. S11,† and the latter also promote the stacking along the *a*-axis.

The case of SFX-2′-Cz is entirely different from the above 2D packing motifs. As all the supramolecular forces are contributed by SFX, an inverted stacking is adopted with SFX sandwiched in the middle and unattractive Cz suspended outboard (Fig. 3c). SFX-2′-Cz is strung along the [100] direction straightly by C–H···π interaction (2.81 Å in distance), while the molecules in the [010] direction present a zigzag stacking with the C–H···O interaction (2.50 Å in distance). There are no obvious supramolecular interactions along the *c*-axis and the zigzag chains are interlaced and embedded with each other to form the arrangement in the *bc* plane, as shown in Fig. S12.† The interaction energy (IE) calculation[20] results (Table S2†) of the two dimers (marked in Fig. 3c by rectangles) indicate that the predominant driving force during the molecular assembly process is the C–H···π interaction and leads to a 1D nanostructure.

To investigate how the tuning of molecular arrangements influences the emission process, the photoluminescence (PL) properties of the isomers in dilute solution and nanocrystal suspension are revealed in Fig. 4. It can be found that their intrinsic monomer emissions in dilute solution are similar in peak positions, as 352 nm/364 nm for SFX-2-Cz; 349 nm/364 nm for SFX-3′-Cz and 352 nm/365 nm for SFX-2′-Cz, indicating their analogous electronic structures and bandgaps. On changing molecular packing motifs and weak interactions, transformations of the emission in the aggregation state have occurred to a different extent. Only slight differences in the relative intensities and positions of the emission peaks are observed for SFX-3′-Cz and SFX-2′-Cz nanocrystals, which can be attributed to the molecular aggregation.[21] However in the spectrum of SFX-2-Cz nanocrystals, apart from the intrinsic

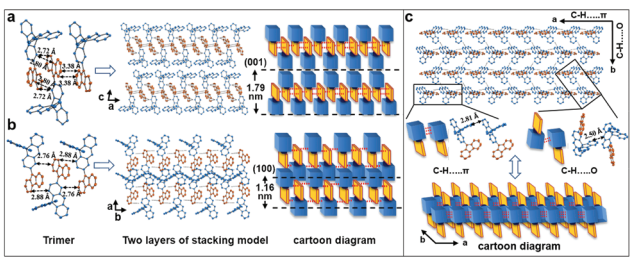

Fig. 3 Molecular packings of SFX-2-Cz, SFX-3′-Cz and SFX-2′-Cz, respectively. (a, b) The representative repeating unit, ordered layer arrangements and the corresponding cartoon diagrams viewed from the *b* and *c* axes of the crystal lattice for SFX-2-Cz and SFX-3′-Cz, respectively. (c) The representative dimer repeating unit in two directions of [100] and [010], the packing of SFX-2′-Cz molecules viewed perpendicular to the *ab* plane and the corresponding cartoon diagram.

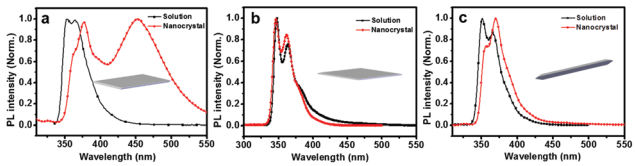

Fig. 4 (a–c) Normalized photoluminescence (PL) emission spectra of SFX-2-Cz, SFX-3′-Cz and SFX-2′-Cz in dilute solution and nanocrystal suspension (excitation wavelength: 327 and 331 nm for SFX-2-Cz, 339 and 343 nm for SFX-3′-Cz, 341 and 352 nm for SFX-2′-Cz in dilute solution and nanocrystal suspension, respectively.) The insets in (a), (b) and (c) show the nanocrystalline morphologies of the three isomers.

emission at 352 nm/364 nm red-shifting to 376 nm with a shoulder peak at 364 nm, a significantly new broad band is emerged at 453 nm, which can be regarded as a typical excimer emission. Combined with similar excitation spectra at 376 nm and 453 nm (Fig. S13†), the corresponding transient PL decay spectra (Fig. S14†) confirm that the 453 nm emission band with a longer lifetime originates from intermolecular excimer emission.[22] The certain π-stacking between Cz segments through the interdigital ILB packing is crucial for the excimer formation (Fig. S15†),[23] which could not be observed in the case of SFX-3′-Cz and SFX-2′-Cz, elucidating that the precise modulation of the molecular arrangement regulates the exciton behaviors effectively.

In summary, three isomers with SFX and Cz connected at different linkage sites were designed to explore the multiple roles of the same segment during the self-assembly process. SFX can act as a pure bulky group, or a difunctional group with both supramolecular and steric features. In a word, the supramolecular interaction sites on SFX or Cz are variable and lead to three SMART molecular models: SS–BG molecule, SS–SBG molecule and PS–SBG molecule. An evolution of the corresponding molecular packing mode was realized from interdigital ILB packing to interstratified ILB packing to SFX-string stacking, accompanied by the change of nanocrystal morphology and PL properties. Instead of proposing isolated cases, this work tries to classify the segments' roles and create proof-of-concept model molecules with the SMART strategy for rational molecular design and assembly behavior forecast.

Conflicts of interest

There are no conflicts to declare.

Acknowledgements

The project was supported by the National Natural Science Foundation of China (61604081, 61605090, and U1301243), the Natural Science Foundation of the Jiangsu Higher Education Institutions (16KJB430023), the Doctoral Fund of the Ministry of Education of China (20133223110007), the Excellent Science and Technology Innovation Team of Jiangsu Higher Education Institutions (2013), the Natural Science Foundation of Jiangsu Province, China (BM2012010), the Peaks Project of Jiangsu Province (XCL-CXTD-009), a project funded by the Priority Academic Program Development of Jiangsu Higher Education Institutions, PAPD (YX03002), NUPTSF (NY215055, NY215061), and National Key Basic Research Program of China (2015CB932202).

Notes and references

1 (*a*) H. Nie, B. Chen, J. Zeng, Y. Xiong, Z. Zhao and B. Z. Tang, *J. Mater. Chem. C*, 2018, **6**, 3690–3698; (*b*) Z. Y. Yu, Y. S. Wu, L. Xiao, J. W. Chen, Q. Liao, J. N. Yao and H. B. Fu, *J. Am. Chem. Soc.*, 2017, **139**, 6376–6381; (*c*) X. D. Wang, H. Li, Y. S. Wu, Z. Z. Xu and H. B. Fu, *J. Am. Chem. Soc.*, 2014, **136**, 16602–16608.

2 (*a*) Y. L. Lei, Q. Liao, H. B. Fu and J. N. Yao, *J. Am. Chem. Soc.*, 2010, **132**, 1742–1743; (*b*) A. L. Tang, C. L. Zhan, J. N. Yao and E. J. Zhou, *Adv. Mater.*, 2017, **29**, 1600013; (*c*) Z. Z. Li, L. S. Liao and X. D. Wang, *Small*, 2018, **14**, 1702952.

3 (*a*) T. S. Chu and Y. Liu, *Org. Electron.*, 2017, **53**, 165–184; (*b*) L. Wang, Y. S. Wu, J. W. Chen, L. F. Wang, Y. P. Liu, Z. Y. Yu, J. N. Yao and H. B. Fu, *J. Phys. Chem. Lett.*, 2017, **8**, 5609–5615; (*c*) Y. Jiao, J. F. Xu, Z. Q. Wang and X. Zhang, *ACS Appl. Mater. Interfaces*, 2017, **9**, 22635–22640.

4 D. B. Xiao, L. Xi, W. S. Yang, H. B. Fu, Z. G. Shuai, Y. Fang and J. N. Yao, *J. Am. Chem. Soc.*, 2003, **125**, 6740–6745.

5 J. Li, D. X. Ding, Y. T. Tao, Y. Wei, R. F. Chen, L. H. Xie, W. Huang and H. Xu, *Adv. Mater.*, 2016, **28**, 3122–3130.

6 L. Shan, D. Q. Liu, H. Li, X. M. Xu, B. W. Shan, J. B. Xu and Q. Miao, *Adv. Mater.*, 2015, **27**, 3418–3423.

7 G. Schweicher, V. Lemaur, C. Niebel, C. Ruzie, Y. Diao, O. Goto, W. Y. Lee, Y. Kim, J. B. Arlin, J. Karpinska, A. R. Kennedy, S. R. Parkin, Y. Olivier, S. C. Mannsfeld, J. Cornil, Y. H. Geerts and Z. N. Bao, *Adv. Mater.*, 2015, **27**, 3066–3072.

8 (*a*) M. M. Payne, S. R. Parkin, J. E. Anthony, C. C. Kuo and T. N. Jackson, *J. Am. Chem. Soc.*, 2005, **127**, 4986–4987; (*b*) J. H. Chen, C. K. Tee, M. Shtein, D. C. Martin and J. Anthony, *Org. Electron.*, 2009, **10**, 696–703.

9 E. Elacqua, P. T. Jurgens, J. Baltrusaitis and L. R. MacGillivray, *CrystEngComm*, 2012, **14**, 7567–7571.

10 Z. Q. Xie, B. Yang, F. Li, G. Cheng, L. L. Liu, G. D. Yang, H. Xu, L. Ye, M. Hanif, S. Y. Liu, D. G. Ma and Y. G. Ma, *J. Am. Chem. Soc.*, 2005, **127**, 14152–14153.

11 Y. S. Zhao, *Organic Nanophotonics: Fundamentals and Applications*, Springer-Verlag, Berlin, Heidelberg, 2015.

12 W. Yao, Y. L. Yan, L. Xue, C. Zhang, G. P. Li, Q. D. Zheng, Y. S. Zhao, H. Jiang and J. N. Yao, *Angew. Chem. Int. Ed.*, 2013, **52**, 8713–8717.

13 K. Balakrishnan, A. Datar, T. Naddo, J. L. Huang, R. Oitker, M. Yen, J. C. Zhao and L. Zang, *J. Am. Chem. Soc.*, 2006, **128**, 7390–7398.

14 (*a*) Y. B. Wang, H. B. Fu, A. D. Peng, Y. S. Zhao, J. S. Ma, Y. Ma and J. N. Yao, *Chem. Commun.*, 2007, 1623–1625; (*b*) Y. Xiong, Z. Zhao, W. J. Zhao, H. L. Ma, Q. Peng, Z. K. He, X. P. Zhang, Y. C. Chen, X. W. He and B. Z. Tang, *Angew. Chem. Int. Ed.*, 2018, **57**, 7997–8001.

15 J. C. Xiao, X. Y. Xiao, Y. L. Zhao, B. Wu, Z. Y. Liu, X. M. Zhang, S. J. Wang, X. H. Zhao, L. Liu and L. Jiang, *Nanoscale*, 2013, **5**, 5420–5425.

16 M. B. Avinash and T. Govindaraju, *Adv. Funct. Mater.*, 2011, **21**, 3875–3882.

17 L. H. Xie, C. R. Yin, W. Y. Lai, Q. L. Fan and W. Huang, *Prog. Polym. Sci.*, 2012, **37**, 1192–1264.

18 Z. Q. Lin, J. Liang, P. J. Sun, F. Liu, Y. Y. Tay, M. D. Yi, K. Peng, X. H. Xia, L. H. Xie, X. H. Zhou, J. F. Zhao and W. Huang, *Adv. Mater.*, 2013, **25**, 3664–3669.

19 Y. X. Li, S. S. Wang, Y. Yu, H. Zhang, W. Y. Wang, R. Q. Yang, L. H. Xie, F. Liu, Z. Q. Lin, N. E. Shi, L. T. Sun and W. Huang, *Small*, 2018, **14**, 1703151.

20 (*a*) M. Reza Afyouni, H. Farrokhpour and A. Najafi Chermahini, *Comput. Theor. Chem.*, 2016, **1094**, 42–46; (*b*) Y. M. Liu, Y. C. Liu, A. A. Gallo, K. D. Knierim, E. R. Taylor and N. Tzeng, *J. Mol. Struct.*, 2015, **1084**, 223–228.

21 A. Patra, S. P. Anthony and T. P. Radhakrishnan, *Adv. Funct. Mater.*, 2007, **17**, 2077–2084.

22 (*a*) C. J. Ou, B. Y. Ren, J. W. Li, D. Q. Lin, C. Zhong, L. H. Xie, J. F. Zhao, B. X. Mi, H. T. Cao and W. Huang, *Org. Electron.*, 2017, **43**, 87–95; (*b*) J. Lee, B. Kim, J. E. Kwon, J. Kim, D. Yokoyama, K. Suzuki, H. Nishimura, A. Wakamiya, S. Y. Park and J. Park, *Chem. Commun.*, 2014, **50**, 14145–14148.

23 T. Hinoue, Y. Shigenoi, M. Sugino, Y. Mizobe, I. Hisaki, M. Miyata and N. Tohnai, *Chem. Eur. J*, 2012, **18**, 4634–4643.